

Breather stripes and radial breathers of the two-dimensional sine-Gordon equation

P. G. Kevrekidis,^{1,2} R. Carretero-González,³ J. Cuevas-Maraver,^{4,5}
D. J. Frantzeskakis,⁶ J.-G. Caputo,^{7,*} and B. A. Malomed^{8,9,†}

¹*Department of Mathematics and Statistics, University of Massachusetts Amherst, Amherst, MA 01003-4515, USA*

²*Mathematical Institute, University of Oxford, Oxford, OX2 6GG, UK*

³*Nonlinear Dynamical Systems Group,[‡] Computational Sciences Research Center,
and Department of Mathematics and Statistics, San Diego State University, San Diego, California 92182-7720, USA*

⁴*Grupo de Física No Lineal, Universidad de Sevilla. Departamento de Física Aplicada I,
Escuela Politécnica Superior, C/ Virgen de África, 7, 41011 Sevilla, Spain*

⁵*Instituto de Matemáticas de la Universidad de Sevilla. Avda. Reina Mercedes, s/n. Edificio Celestino Mutis, 41012 Sevilla, Spain*

⁶*Department of Physics, National and Kapodistrian University of Athens, Panepistimiopolis, Zografos, Athens 15784, Greece*

⁷*Laboratoire de Mathématiques, INSA de Rouen Normandie
76801 Saint-Etienne du Rouvray, France.*

⁸*Department of Physical Electronics, School of Electrical Engineering,
Faculty of Engineering, Tel Aviv University, Tel Aviv 69978, Israel*

⁹*Instituto de Alta Investigación, Universidad de Tarapacá, Casilla 7D, Arica, Chile*

We revisit the problem of transverse instability of a 2D breather stripe of the sine-Gordon (sG) equation. A numerically computed Floquet spectrum of the stripe is compared to analytical predictions developed by means of multiple-scale perturbation theory showing good agreement in the long-wavelength limit. By means of direct simulations, it is found that the instability leads to a breakup of the quasi-1D breather in a chain of interacting 2D radial breathers that appear to be fairly robust in the dynamics. The stability and dynamics of radial breathers in a finite domain are studied in detail by means of numerical methods. Different families of such solutions are identified. They develop small-amplitude spatially oscillating tails (“nanoptera”) through a resonance of higher-order breather’s harmonics with linear modes (“phonons”) belonging to the continuous spectrum. These results demonstrate the ability of the 2D sG model within our finite domain computations to localize energy in long-lived, self-trapped breathing excitations.

PACS numbers:

I. INTRODUCTION

One of the most influential models in studies of solitary waves is the sine-Gordon (sG) equation, which has been extensively explored in numerous volumes [1–3] and reviews [4]. The one-dimensional (1D) version is the first nonlinear equation whose integrability was found (in the form of the Bäcklund transform, ca. 140 years ago [5]). Later, its complete integrability was systematically investigated by means of the inverse scattering transform (IST) [6]. Commonly known exact solutions to the sG equation are topological kink solitons and kink-antikink bound states in the form of breathers. Modes of the latter type are uncommon in continuum systems, but find broad realizations in their discrete counterparts [7, 8].

While the 1D sG equation has become a textbook etalon of integrable models, far less is known about higher dimensional versions of the same equation, which are not integrable by the IST. In particular, some effort has been dedicated to the kinematics and dynamics of kinks in two and three dimensions (2D and 3D) [9–12], including their ability to produce breathers as a result of collisions with boundaries [13], and proneness to be stably pinned by local defects [14].

Nevertheless, despite the relevance of physical realizations

of the sG model in higher dimensions (see, e.g., Ref. [15] for a recent example), the study of breathers in such settings was scarce. While effective equations of motion for breathers were derived long ago [16], these equations do not apply to steady isotropic breather profiles. Thus, it remains unknown at present whether such robust solutions may exist indefinitely long, or they eventually decay.

Moreover, there is a relevant related question concerning quasi-1D breather solutions in the higher-dimensional problem, i.e., breather stripes and planes in the 2D and 3D settings, respectively. The seminal work of Ref. [17] had predicted that such quasi-1D solutions are subject to transverse instabilities. This is a natural property due to the relation of the sG model, in the limit when it produces broad small-amplitude breathers, to the nonlinear Schrödinger (NLS) equation [1, 2], in which both bright and dark quasi-1D solitons are prone to transverse instabilities [18] —see, e.g., theoretical work of Ref. [19] and Refs. [20–22] for experimental realizations in atomic and optical physics. On the other hand, quasi-1D sG kinks are *not* vulnerable to the transverse instability. In this work, we aim to further explore the dynamics of quasi-1D sG breathers in the 2D geometry, including their transverse instability and its development into radially shaped breathing modes.

We start the analysis by revisiting the key result of Ref. [17] for quasi-1D breathers in the 2D sG equation. We test this result for breathers with different frequencies ω_b and demonstrate that their instability in the long-wavelength limit is accurately captured by the analytical treatment. Our numerical calculation of the respective Floquet multipliers (FMs) ad-

[‡]URL: <http://nlds.sdsu.edu>

*Email: caputo@insa-rouen.fr

†Email: malomed@tauext.tau.ac.il

ditionally permits the systematic identification of spectra of transverse-instability modes as a function of the corresponding perturbation wavenumber, k_y . These results indicate that the quasi-1D sG breathers do not only maintain a main band of unstable wavenumbers, similarly to what is known for the NLS equation, where only a band of low wavenumbers is unstable. Importantly, they also display, for appropriate frequencies ω_b , instability bubbles for higher wavenumbers. Near the NLS limit of $\omega_b \rightarrow 1$, we demonstrate how the NLS reduction, as well as a novel, to the best of our knowledge, variational approximation involving the transverse degree of freedom are able to capture instability and dynamical features, including the basic necking phenomenon occurring in the course of the breather stripe's evolution.

Studying the dynamics ensuing from the generic long-wavelength instabilities of the breather stripes, we identify spontaneous formation of localized breather waveforms. Further, “naively” initializing a quasi-1D radial breather profile, with x replaced by the radial variable, r , we find that the solutions adjust themselves and their frequencies in the course of a transient stage of the evolution, to form potentially very long-lived localized modes trapping the energy in a localized spatial region. This finding motivates us to study the radial time-periodic breathers, which we are able to find, as genuine steady states over a period, using fixed-point iteration techniques. Stability of these radial breathers is studied numerically in the framework of the Floquet theory.

The manuscript is organized as follows. Section II reports the results concerning the breather stripes. In particular we expand the instability results for the stripes from Ref. [17]. The results, which are valid from the long-wavelength limit to larger wavenumbers, are obtained by connecting the sG dynamics to the NLS limit, using multiple-scale expansions, and also by dint of a variational approach, which is relevant for large ω_b . We present numerical results demonstrating that the development of the breather-stripe instability nucleates long-lived radial breathers. The existence and stability of such radial breathers is the subject of Sec. III. Finally, in Sec. IV we present a summary of the results, concluding remarks, and point out avenues for further research.

II. BREATHER STRIPES

A. Modulational instability of breather stripes

The sG equation is a special case of the more general Klein-Gordon class of models which in 2D is written as

$$u_{tt} - \nabla^2 u + V'(u) = 0, \quad (1)$$

where $u(x, y, t)$ is a real field depending on coordinates (x, y) and time t , subscripts with respect to the independent variables denote partial derivatives, and $V(u)$ is the potential that defines the particular model. The most studied among these models pertain to $V(u) = 1 - \cos(u)$ and $V(u) = (u^2 - 1)^2/2$, which are referred to as the sG [3] and “ ϕ^4 ” [23] equations, respectively. From now on, we focus on the former one:

$$u_{tt} - \nabla^2 u + \sin u = 0. \quad (2)$$

The 1D version of the sG equation admits commonly known kink/antikink and breather solutions. Kinks are (generally speaking, traveling) 1D profiles that asymptote to the uniform background states, $u_{\pm\infty} = \{0, 2\pi\}$, of the form

$$u_k = 4 \arctan \left[\exp \left(s(x - ct) / \sqrt{1 - c^2} \right) \right], \quad (3)$$

where $s = \pm 1$ is the topological charge, which distinguishes kinks and antikinks, and c is the velocity, which may take values $|c| < 1$. On the other hand, breathers correspond to profiles which are oscillatory in time and localized in space. In particular, the exact 1D sG breather solution is

$$u_b(x, t) = 4 \tan^{-1} \left[\frac{\beta}{\omega_b} \operatorname{sech}(\beta x) \cos(\omega_b t) \right], \quad (4)$$

where $\beta \equiv \sqrt{1 - \omega_b^2}$ and the band of the breather frequencies is $0 \leq \omega_b < 1$.

In the spirit of the work done in Ref. [14] for a kink stripe, we consider the transverse instability of the breather stripe

$$u_{2D}(x, y, t) = u_b(x, t). \quad (5)$$

We then perturb the breather stripe according to

$$u(x, y, t) = u_b(x, t) + w(x, y, t)$$

where the perturbation w is assumed small. Enforcing this solution to satisfy Eq. (2) yields, to first order, the following evolution equation for the perturbation:

$$w_{tt} - (w_{xx} + w_{yy}) + \cos(u_b(x, t))w = 0. \quad (6)$$

This equation is a linear, inhomogeneous in x , wave equation so that we can study each transverse wave number k_y separately and assume

$$w(x, y, t) = \xi(x, t) \exp(ik_y y), \quad (7)$$

where $\xi(x, t)$ describes the x -dependent shape (eigenmode) of the perturbation. Plugging (7) into (6), yields

$$\xi_{tt} - \xi_{xx} + (k_y^2 + \cos(u_b(x, t)))\xi = 0. \quad (8)$$

This is a periodically forced wave equation and can be solved using Floquet theory, see Appendix for details. The final result is the linear operator \mathcal{M}

$$\begin{pmatrix} \{\xi(x, T)\} \\ \{\xi_t(x, T)\} \end{pmatrix} = \mathcal{M} \begin{pmatrix} \{\xi(x, 0)\} \\ \{\xi_t(x, 0)\} \end{pmatrix}, \quad (9)$$

relating the solutions of Eq. (8) at $t = 0$ and $t = T$. If the maximal Floquet multiplier Λ (obtained from the eigenvalues of \mathcal{M}) is such that $|\Lambda| > 1$, ξ will grow and the stripe will be unstable. In the case of instability (where at least one eigenvalue has modulus larger than 1) the eigenmode ψ corresponding to the maximum $|\Lambda|$ gives the solution $\xi(x, t)$ and the modulation of the stripe through its perturbation $w(x, y, t)$.

In the seminal work of Ref. [17], Ablowitz and Kodama (AK) predicted that, in the long-wavelength limit, breather

stripes are subject to modulational instability (MI). Their main result provides the instability growth rate λ for the stripe, as a function of the perturbation wavenumber, k_y :

$$\lambda = \sigma k_y, \quad \sigma^2 = \frac{\sqrt{1 - \omega_b^2}}{\omega_b} \arcsin \left(\sqrt{1 - \omega_b^2} \right). \quad (10)$$

Given that the AK result is valid in the $k_y \rightarrow 0$ limit, we wish to investigate the instability for larger values of k_y . To this end, one needs to solve Eq. (8) numerically, by means of a suitable fixed-point method (see details in the Appendix), taking into regard that a finite size (and a finite discretization parameter) of the solution domain induces gaps in the spectrum of the linear modes and, also that breathers may feature modified tails generated by “hybridization” (mixing) of the third and higher-order odd harmonics with linear modes (“phonons”), reminiscent of the formation of the so-called “nanoptera” in the ϕ^4 equation [3]. The hybridization depends on the location of the linear modes, which, in turn, depends on the specifics of the domain size and boundary conditions. We have used periodic boundary conditions in domain involving $x \in [-L_x, L_x)$ with $L_x = 100$ and computed the periodic steady states corresponding to zero initial velocity $u_t(x, y, t = 0) = 0$. Finally, it is important to note that, addressing the dynamics with the underlying time-periodic solution, one needs to resort to Floquet analysis and the computation of FMs, in order to extract the (in)stability eigenvalues (see details in Appendix). The FMs, Λ , are translated into (in)stability eigenvalues λ (in particular, for the comparison to the AK theory), via $\Lambda = \exp(\lambda T)$, where $T = 2\pi/\omega_b$ is the breather’s period.

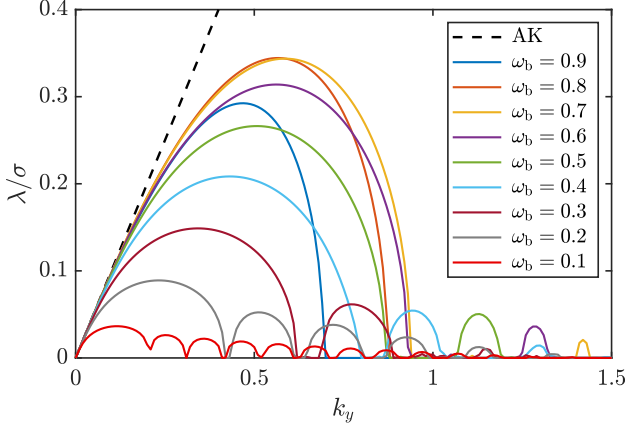


FIG. 1: (Color online) Modulational-instability eigenvalues for the breather stripe vs. wavenumber k_y of the modulational perturbations, for the indicated values of the breather’s frequency. Solid curves depict the eigenvalues numerically determined by unstable Floquet multipliers (see the text). The dashed line represents the analytical Ablowitz-Kodama (AK) result for the long-wavelength limit, $k_y \rightarrow 0$ [17], given by Eq. (10).

Figure 1 depicts the dependence on k_y of the MI growth rate for selected values of the breather stripe’s frequency, ω_b . The eigenvalues have been rescaled by σ [see Eq. (10)] to facilitate the comparison to the AK analytical prediction, given

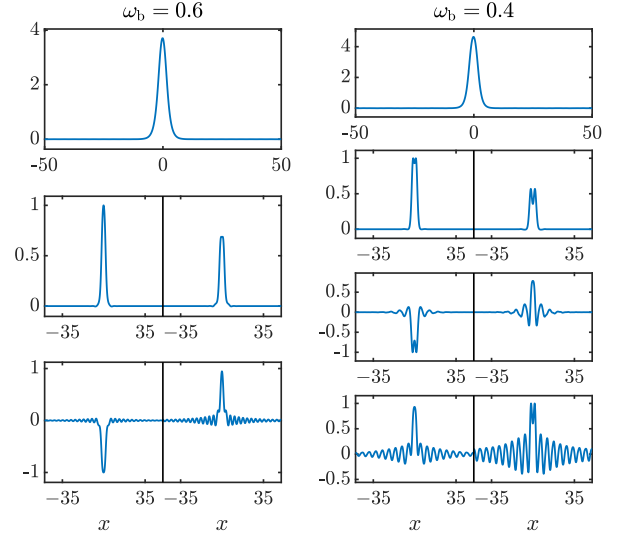


FIG. 2: (Color online) Snapshots of the breathers $u_b(x, t = 0)$ and corresponding eigenfunctions ψ for different MI windows/bubbles. The left and right sets of panels correspond to $\omega_b = 0.6$ and $\omega_b = 0.4$, respectively. Snapshots of the breathers $u_b(x, t = 0)$ are displayed in the top panels. The subsequent ones, from top to bottom, display the u (left) and u_t (right) components of the eigenfunctions ψ corresponding to the highest-MI wavenumbers in the bubbles of Fig. 1. For $\omega_b = 0.6$, two MI bubbles exist (with maxima located at $k_y \approx 0.57$ and 1.28), while for $\omega_b = 0.4$ there are three MI bubbles (with maxima located at $k_y \approx 0.43$, 0.94 and 1.30). The computation domain is $x \in [-100, 100)$, half of which is shown here.

by Eq. (10) and shown by the dashed line in the figure. The MI spectrum indeed follows the AK prediction as $k_y \rightarrow 0$, for all values of ω_b , i.e., for long perturbation wavelengths, the MI eigenvalue is $\lambda/\sigma \approx k_y$, independent of ω_b . Further, Fig. 1 demonstrates that, beyond the AK limit, λ grows with k_y until reaching a maximum, and then decreases, falling to zero at some $k_y = \tilde{k}_y$. We refer to this first instability window ($0 < k_y < \tilde{k}_y$) as the main MI “bubble”. The value \tilde{k}_y , as well as the maximum of λ/σ , increase with ω_b for $\omega_b \leq 0.7$, but this trend changes to a decrease for $0.7 < \omega_b < 1$. This result, which is in stark contrast with properties of MI for the NLS equation [24, 25], has its origin in increasing contributions from the third and higher harmonics of the breather’s oscillatory waveform when $\sqrt{1 - \omega_b^2}$ decreases and, consequently, truncating at the first harmonic is no longer a good approximation for expression (4) for $\omega_b \lesssim 0.7$.

Furthermore, beyond the main MI bubble, Fig. 1 suggests another noteworthy feature: the existence of secondary MI bubbles for $k_y > \tilde{k}_y$. These secondary bubbles get narrower and more spaced with the increase of ω_b ; in fact, they are not found for $\omega_b > 0.7$. To understand MI in the secondary bubbles, and to compare it to the main MI window, $k_y < \tilde{k}_y$, we explore the shape of the corresponding eigenfunctions of the modulational perturbations. In particular, Fig. 2 depicts the breather profile and eigenfunctions corresponding to unstable eigenvalues in the main MI window and secondary bubbles for $\omega_b = 0.6$ and $\omega_b = 0.4$. In the case of $\omega_b = 0.6$ (the set of

left panels in the figure), MI takes place in the main window and in one secondary bubble, while in the case of $\omega_b = 0.4$ (the set of right panels) two secondary MI bubbles are present. All perturbation eigenfunctions in these MI bubbles are real as the corresponding eigenvalue Λ responsible for the instability is also real (we depict the respective components u and u_t in the left and right plots, respectively). Figure 2 exhibits eigenfunctions that bear qualitatively similar shapes. Namely, the eigenfunctions in the main MI window are all localized without oscillating tails, while in the secondary bubbles, tails are attached to the core of the eigenfunctions, getting stronger in higher-order bubbles.

B. Connection to NLS

To better understand the MI spectrum for the breather stripes, we may use the connection between the sG and the NLS equations, in the limit of $\omega_b \rightarrow 1$. Such a connection can be accurately established via the multiple-scales perturbation method [26]. Below we will briefly present the methodology and provide the main results (see also Refs. [1, 2] for a detailed analysis). First we note that, in the limit of $\omega_b \rightarrow 1$, the sG breather of Eq. (4) has a small amplitude and, hence, one can expand the sG nonlinearity as $\sin u \approx u - u^3/6$. Thus, we seek for solutions of the resulting ϕ^4 -equation in the form of the asymptotic expansion:

$$u(x, t) = \sum_{n=1}^N \epsilon^n u_n(x_0, \dots, x_N, t_0, \dots, t_N), \quad (11)$$

where u_n are functions of the independent variables $x_j = \epsilon^j x$ and $t_j = \epsilon^j t$ ($j = 0, 1, 2, \dots, N$), while $0 < \epsilon \ll 1$ is a formal small parameter. Substituting ansatz (11) in the equation, and collecting coefficients in front of different powers of ϵ yields a set of equations, the first three ones being

$$O(\epsilon^1) : \mathcal{L}_0 u_1 = 0, \quad (12)$$

$$O(\epsilon^2) : \mathcal{L}_0 u_2 + \mathcal{L}_1 u_1 = 0, \quad (13)$$

$$O(\epsilon^3) : \mathcal{L}_0 u_3 + \mathcal{L}_1 u_2 + \mathcal{L}_2 u_1 - \frac{1}{6} u_1^3 = 0. \quad (14)$$

where

$$\mathcal{L}_0 \equiv \partial_{t_0}^2 - \partial_{x_0}^2 + 1,$$

$$\mathcal{L}_1 \equiv 2(\partial_{t_0} \partial_{t_1} - \partial_{x_0} \partial_{x_1}),$$

$$\mathcal{L}_2 \equiv \partial_{t_1}^2 - \partial_{x_1}^2 + 2(\partial_{t_0} \partial_{t_2} - \partial_{x_0} \partial_{x_2}).$$

To leading order, $O(\epsilon)$, the solution to Eq. (12) is

$$u_1 = A(x_1, x_2, \dots, t_1, t_2, \dots) \exp(i\Phi) + \text{c.c.}, \quad (15)$$

where A is a yet-to-be-determined function of the slow variables, c.c. stands for the complex conjugate, and $\Phi = kx_0 - \omega t_0$, with wavenumber k and frequency ω obeying the linear dispersion relation,

$$\omega^2 = k^2 + 1. \quad (16)$$

Substituting solution (15) in Eq. (13), it is evident that the second term is secular and has to be removed. This yields equation $A_{t_1} + v_g A_{x_1} = 0$, where the $v_g = k/\omega$ is the sG group velocity, as per Eq. (16). This result suggests that the amplitude function A depends on variables x_1 and t_1 only through a traveling coordinate,

$$X = x_1 - v_g t_1, \quad (17)$$

i.e., $A = A(X, x_2, x_3, \dots, t_2, t_3, \dots)$. Furthermore, as concerns the solution of Eq. (13) [which is now reduced to $\mathcal{L}_0 u_2 = 0$], we take the trivial solution $u_2 = 0$, because a nontrivial one would be of the form as Eq. (15), hence its amplitude function can be included in field A . Finally, at the next order, $O(\epsilon^3)$, upon substituting u_1 from Eq. (15) and $u_2 = 0$, Eq. (14) becomes:

$$\begin{aligned} \mathcal{L}_0 u_3 = & [(1 - v_g^2) A_{XX} + 2i\omega (A_{t_2} + v_g A_{x_2})] \exp(i\theta) \\ & + \frac{1}{6} A^3 \exp(3i\theta) + \frac{1}{2} |A|^2 A \exp(i\theta) + \text{c.c.} = 0. \end{aligned} \quad (18)$$

It is observed that secular terms $\propto \exp(i\theta)$ arise on the right-hand side of Eq. (18) [term $\propto \exp(3i\theta)$ is not secular, because it is out of resonance with the uniform solution]. Removing the secular terms leads to the following NLS equation for complex amplitude A :

$$iA_{t_2} + (2\omega^3)^{-1} A_{XX} + (4\omega)^{-1} |A|^2 A = 0, \quad (19)$$

where we have removed the group-velocity term by redefining $x_2 \mapsto x_2 - v_g t_2$, and made use of identity $1 - v_g^2 = 1/\omega^2$, resulting from Eq. (16).

The fact that the NLS equation (19) is valid in the band $\omega \geq 1$, according to Eq. (16), allows us to consider the limit of $\omega \rightarrow 1$, i.e., $k \rightarrow 0$. In this case, with the vanishing group velocity $v_g \rightarrow 0$, variable X , defined by Eq. (17), carries over into x_1 , Eq. (19) reduces to the form of

$$iA_{t_2} + (1/2)A_{x_1 x_1} + (1/4)|A|^2 A = 0. \quad (20)$$

The stationary soliton solution of the reduced NLS, expressed in terms of original variables x and t , is

$$A = \eta \operatorname{sech}[(1/2)(\epsilon\eta x)] \exp[(i/8)\epsilon^2\eta^2 t], \quad (21)$$

where η is an arbitrary $O(1)$ parameter. Thus, an approximate sG breather solution, valid up to order $O(\epsilon)$ near the edge of the phonon band, is produced by Eqs. (15) and (21):

$$u(x, t) \approx 2\epsilon\eta \operatorname{sech}\left(\frac{1}{2}\epsilon\eta x\right) \cos\left[\left(1 - \frac{1}{8}\epsilon^2\eta^2\right)t\right]. \quad (22)$$

Note that the frequency of soliton solution (22), $\omega_s = 1 - (\epsilon^2\eta^2/8)$, is *smaller* than the cutoff frequency, $\omega = 1$, which naturally means that this self-trapped excitation belongs to the phonon *bandgap*, as is known for the sG breather. This fact indicates strong connection between the stationary NLS soliton and the sG breather in the limit of

$$0 < 1 - \omega_b \ll 1. \quad (23)$$

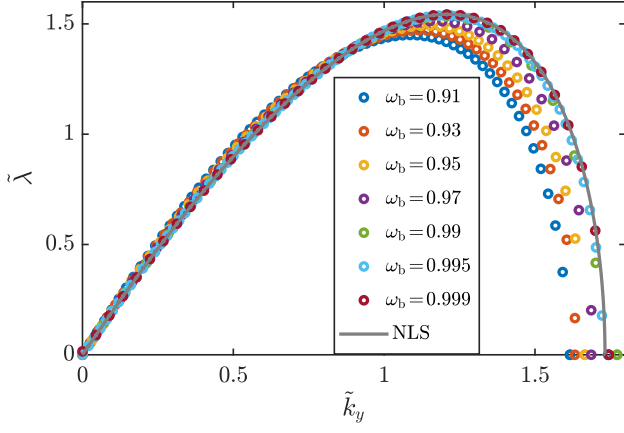


FIG. 3: (Color online) Comparison between the (scaled) instability spectrum of the sG breather stripe (shown by colored dots) and the instability spectrum for a stationary NLS bright-soliton stripe (shown by the gray solid line, as per Refs. [24, 25]). The wavenumber and instability growth rate are rescaled as: $\tilde{k}_y \equiv k_y / \sqrt{1 - \omega_b^2}$ and $\tilde{\lambda} \equiv 2\lambda / (1 - \omega_b^2)$.

Indeed, in this limit, observing that the argument of \tan^{-1} in solution (4) is small, it may be approximated by $u_b \approx (4\beta/\omega_b) \text{sech}(\beta x) \cos(\omega_b t)$. Then, letting $\epsilon\eta \equiv 2\beta$, which means that $\omega_b \approx 1 - (\epsilon^2\eta^2/8) \equiv \omega_s$, we see that the approximate NLS soliton solution, given by Eq. (22), is identical to the sG breather in the limit case defined by Eq. (23). Accordingly, it is expected that the breather stripe's dynamics can be adequately approximated by the NLS equation (19), where ω is identified as the breather stripe's frequency, ω_b .

In particular, the connection between the NLS equation and the sG stripe allows us to approximate the stability spectrum of the sG breather stripe by that for the NLS bright-soliton stripes, which was studied in detail previously [24, 25, 27]. Specifically, in Fig. 3 we compare the rescaled numerically computed instability spectra of the sG breather stripe (dots) for different breather frequencies from region (23) with those for a stationary NLS bright-soliton stripe, taken from Refs. [24, 25]. It is evident that, in the limit of $\omega_b \rightarrow 1$, the (scaled) instability spectrum of the sG stripe indeed smoothly approaches its NLS counterpart.

C. Variational approach for large frequencies

In this Section we present a study of the evolution of sG breather stripes, based on the variational approximation, which is valid for relatively large breather's frequencies. To this end, we note that the 2D sG equation (2) can be derived from the Lagrangian, $L = \iint \mathcal{L} dx dy$, with density

$$\mathcal{L} = \frac{1}{2} (u_t^2 - u_x^2 - u_y^2) - 2 \sin^2\left(\frac{u}{2}\right). \quad (24)$$

We rewrite the exact 1D sG breather solution (4) as

$$u_b = 4 \tan^{-1} [(\tan \mu) \sin(t \cos \mu) \text{sech}(x \sin \mu)], \quad (25)$$

where parameter $\mu \equiv \arcsin(\sqrt{1 - \omega_b^2})$ takes values $0 \leq \mu \leq \pi/2$. We now focus on broad low-amplitude breathers in limit of $\mu \ll \pi/2$, approximating the exact 1D breather (25) by the following *ansatz*:

$$u_b = \chi(y, t) \text{sech}(\mu x). \quad (26)$$

Here, χ is a variational parameter accounting for the possibility of variations of the width of the stripe in the y direction, which may represent the so-called necking instability [27, 28]. According to the VA, evaluating the Lagrangian with *ansatz* (26) substituted in Eq. (24), and deriving the Euler-Lagrange equation from it [29] should yield an effective evolution equation for the width parameter $\chi(y, t)$. In the present form, the Lagrangian density (24) cannot be integrated analytically for *ansatz* (26). Nonetheless, focusing on small-amplitude breather stripes, one may expand the nonlinear term to simplify the Lagrangian density:

$$\mathcal{L} = \frac{1}{2} (u_t^2 - u_x^2 - u_y^2) - \frac{1}{2} u^2 + \frac{1}{24} u^4. \quad (27)$$

Upon substituting *ansatz* (26) in Eq. (27), the integration can be performed in the x direction, yielding the effective Lagrangian:

$$\mu L_{\text{eff}} = \int_{-\infty}^{+\infty} \left(\chi_t^2 - \chi_y^2 - \chi^2 + \frac{1}{18} \chi^4 \right) dy. \quad (28)$$

Finally, the variational equation for $\chi(y, t)$, which governs the evolution of necking perturbations of the sG stripe under the condition (23), is immediately derived from the Lagrangian (28):

$$\chi_{tt} - \chi_{yy} + \left(1 - \frac{\mu^2}{3}\right) \chi - \frac{1}{9} \chi^3 = 0. \quad (29)$$

Before we compare the reduced dynamics, presented by Eq. (29), to the evolution of the full sG breather stripe, we provide a generalization of the VA methodology to incorporate the full nonlinearity of the system. If instead of approximating $\sin(u)$ up to third order as done above, one rewrites the nonlinearity in the effective Lagrangian as $\sin^2(u/2) = (1/2) [1 - \sum_{m=0}^{\infty} (-1)^m u^{2m} / (2m)!]$ and uses the identity,

$$\int_{-\infty}^{+\infty} \text{sech}^{2m}(x) dx = 2^{2m-1} \frac{[(m-1)!]^2}{(2m-1)!}, \quad (30)$$

it is possible to evaluate the effective Lagrangian for the full sinusoidal nonlinearity with *ansatz* (26). The respective extended Euler-Lagrange equation is

$$\chi_{tt} - \chi_{yy} - \frac{\mu^2}{3} \chi - \sum_{m=1}^{\infty} \frac{(-1)^m}{2} \left[\frac{(m-1)!}{(2m-1)!} \right]^2 (2\chi)^{2m-1} = 0. \quad (31)$$

Although Eq. (31) generalizes Eq. (29) in that it takes the full nonlinearity into account, it does not provide an exact theory, because the underlying *ansatz* (26) is only valid for small amplitudes. Thus, the extended equation may provide for a

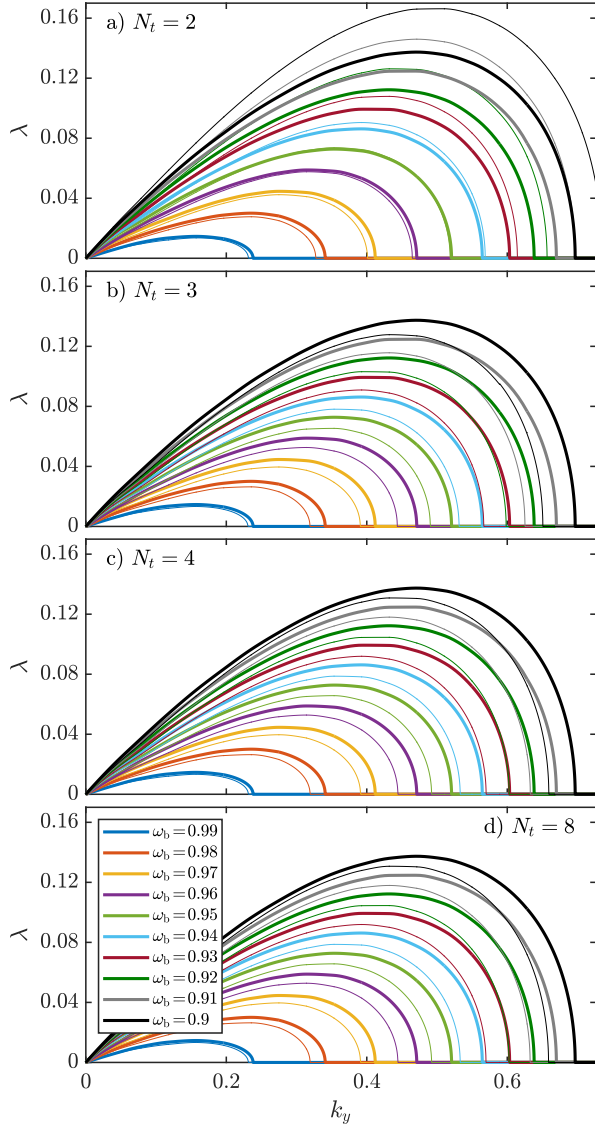


FIG. 4: (Color online) Stability spectra of the sG breather (thick lines) and as produced by reduced model (31) (thin lines) for different breather’s frequencies. The top panel depicts the spectrum produced by Eq. (31) with only $N_t = 2$ [i.e., by Eq. (29)], instead of the infinite sum in the full sG equation. The second, third, and fourth panels display results produced by Eq. (31), keeping $N_t = 3, 4$, and 8, respectively.

a more accurate VA model of the necking dynamics, but this model retains the approximate nature of the above analysis (based on the proposed ansatz).

To gain insight into the validity of the VA models (29) and (31), in Fig. 4 we compare stability spectra provided by these approximations with the numerically found main instability window of the full sG model. Different panels correspond to replacing the infinite sum in Eq. (31) by the truncated sum $\sum_{m=1}^{N_t}$, that keeps the first N_t terms in the expansion. In this notation, Eq. (31) reduces to Eq. (29) when $N_t = 2$. The results presented in Fig. 4 suggest that the MI is indeed ad-

equately captured by the VA in the region (23). This is true qualitatively in that region and even quantitatively as $\omega_b \rightarrow 1$. It is seen too that, as $1 - \omega_b$ increases, the match between the full sG model and its VA counterparts deteriorates. Nonetheless, the VA reproduces the correct overall trend and the shape of the instability spectra. As regards keeping more terms in the expansion of the nonlinearity in the Lagrangian, Fig. 4 shows that proceeding from $N_t = 2$ to $N_t = 3$ does not produce a significant improvement in the accuracy, and there is no discernible difference between $N_t = 4$ and $N_t > 4$ either. Therefore, from now on, we use the simplest reduced model (29) with $N_t = 2$ for the comparison with the full sG model.

D. Dynamical evolution of breather stripes

Having tested the reduced models in terms of the stability spectra, we now extend the comparison by numerically following the necking dynamics in the framework of the full sG model and the VA for a number of scenarios. The evolution was initiated by inputs

$$\begin{aligned} u(x, y, 0) &= u_b(x, 0) \left[1 + \varepsilon \cos \left(\frac{n_y \pi}{L_y} y \right) \right], \\ u_t(x, y, 0) &= 0, \end{aligned} \quad (32)$$

where n_y is the perturbation’s integer mode number (associated with the wavenumber $n_y \pi / L_y$) and ε its relative strength, while $u_b(x, 0)$ is the exact 1D sG breather profile (4). Results of the comparison are depicted in Fig. 5. The dynamics is depicted by means of surface plots of $u(x, y, t)$ at the indicated times. The input was a slightly perturbed exact sG breather stripe, to which one [(a)–(f)] or several [(g) and (h)] perturbation modes with wavenumbers k_y were added as follows. The perturbations were constructed by seeding the necking modulation as per Eq. (32), with perturbation strength $\varepsilon = 0.01$. Panels (a)–(d) depict the comparison for the perturbations with small wavenumbers $n_y = 1, 3, 5$, and 7, corresponding to the necking MI. Panels (e) and (f) correspond to large perturbation wavenumbers, with $n_y = 17$ and $n_y = 19$, which are taken, respectively, just below and above the instability threshold. For the stable case (f) with $n_y = 19$, a stronger perturbation with $\varepsilon = 0.1$ was used to stress the stability of the sG breather against this perturbation wavenumber. Finally, panels (g) and (h) correspond to cases when a mix of perturbation modes with random strengths (chosen in interval $-0.01 \leq \varepsilon \leq 0.01$) is introduced in the initial conditions. Case (g) contains perturbations with modes $1 \leq n_y \leq 5$, while in case (h) we used $1 \leq n_y \leq 22$. In all the cases, to match the underlying oscillation frequencies of the exact breather stripe and its VA counterpart, the time for the VA results is scaled by a fitting factor. This factor, for all the cases shown here, amounts to a reduction of the time between 8 and 10%. As seen in the figure, and as predicted by the stability spectra, perturbations with small wavenumbers always lead to necking MI. The perturbation eventually breaks the stripe into a chain of self-trapped “blobs” (localized modes). These time-oscillating “blobs” are identified as

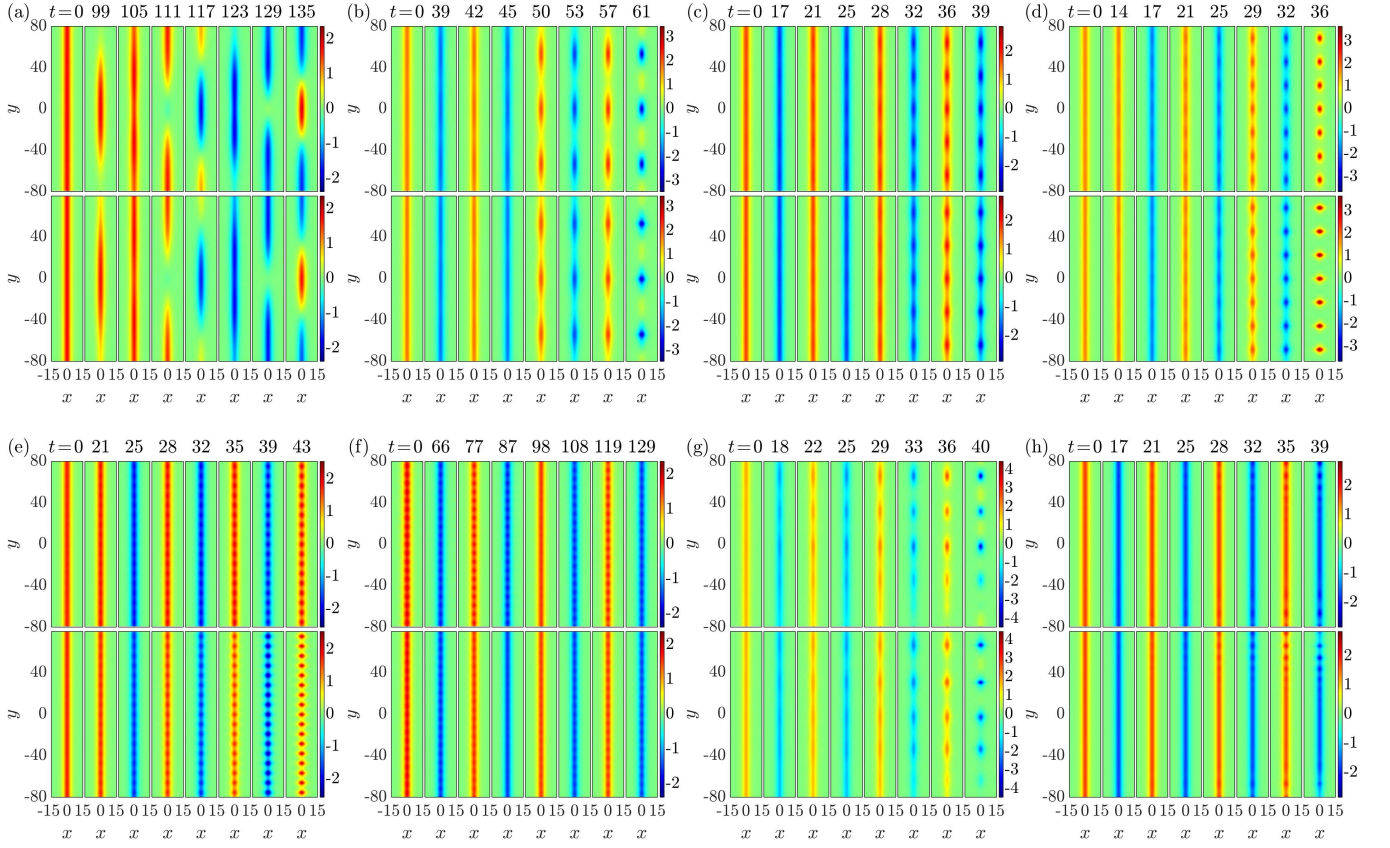


FIG. 5: (Color online) Comparison of the development of the modulational (necking) instability for the sG breather stripe, as produced by the full sG model, and by VA, in the form of Eq. (29), for $\omega_b = 0.9$. The corresponding set of top and bottom subpanels respectively depict the evolution of $u(x, y, t)$ for the full sG dynamics and the VA. The input was a slightly perturbed exact sG breather stripe, to which one [(a)–(f)] or several [(g) and (h)] perturbation modes with wavenumbers k_y are added. The system was integrated in the domain $|x| \leq 40$, $|y| \leq 80$ (only the segment $|x| \leq 15$ is shown), with periodic boundary conditions along y and homogeneous Dirichlet boundary conditions along x . Please see the main text for more details.

highly perturbed radial breathers, this conclusion being the second key aspect of our study (see the following Section III, and also Ref. [13]). All the modes with perturbation indices $1 \leq n_y \leq 17$ ($k_y = n_y \pi / L_y$) [see Eq. (32)] are unstable, and the VA is able to accurately capture the corresponding instability and ensuing dynamics, see panels (a)–(e). Naturally, as the necking perturbation grows, the VA becomes less accurate, as the underlying variational ansatz (26) is no longer an appropriate approximation for the profile of the deformed stripe. Nonetheless, for times up to those at which the stripe breaks into a chain of “blobs”, the VA evolves in tandem with the full sG dynamics. This is also true when, instead of using a single mode as the perturbation, one perturbs the stripe by a collection of modes, as shown in panels (g) and (h) where the perturbations contain, respectively, a combination of the lowest 5 modes and even as many as 22 ones. Finally, in panel (f) of Fig. 5 we present an example of the evolution with the perturbation index ($n_y = 19$) chosen beyond the instability boundary of the main MI window. In this stability case, the simulations demonstrate that the full sG dynamics is closely followed by the VA for longer times, in comparison to the unstable cases.

Figure 6 expands on the results presented in Fig. 5 by considering random perturbation of the breather stripes and allowing the dynamics to evolve for longer times. Interestingly, Fig. 6 shows the formation of robust spatially localized “blobs”. The top row of panels depicts snapshots of the field $u(x, y, t)$ at the indicated moments of time. Since the solutions that we are inspecting are oscillatory in time, in the corresponding bottom row we plot snapshots of the corresponding 2D energy density,

$$\mathcal{E}(x, y, t) = \frac{1}{2} (u_t^2 + u_x^2 + u_y^2) + V(u), \quad (33)$$

which allows us to partially eliminate the oscillations, and thus to better capture the emergence and dynamics of the “blobs” (localized breathers). The figure suggests that the breathers generated by the MI from the unstable stripes are generically robust, although some of them disappear, while others spontaneously emerge from condensation of the background random field. Note that the localized breathers travel and, as a result, collide or merge with neighboring ones. In Fig. 7, we display 3D isocontour plots of the energy density in the (x, y, t) spatiotemporal continuum. This figure makes

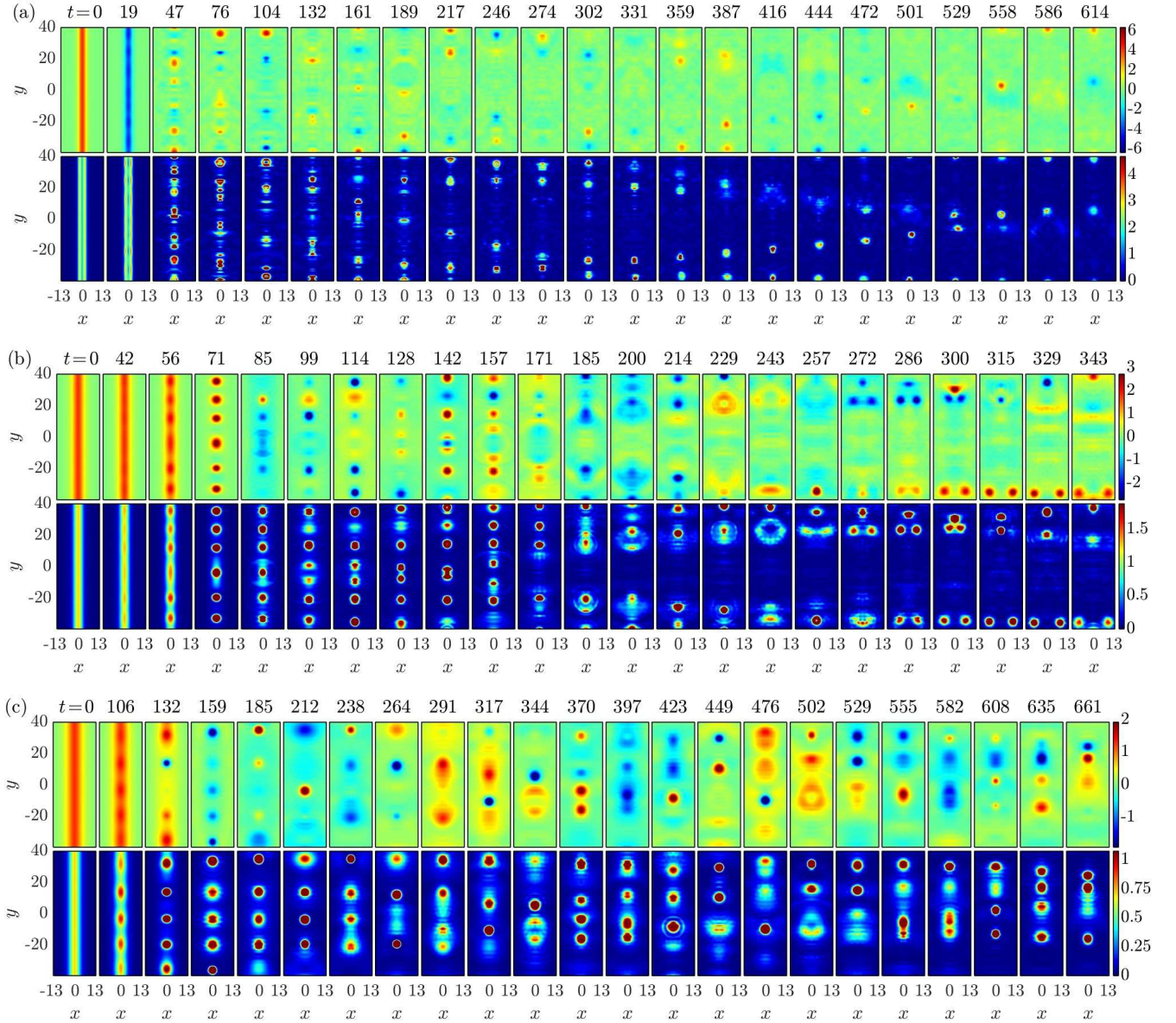


FIG. 6: (Color online) Long term evolution of randomly perturbed breather stripes showing the generation of “blobs” (perturbed radial sG breathers) as a result of necking MI. Depicted is the corresponding field $u(x, y, t)$ and energy density $\mathcal{E}(x, y, t)$ (top and bottom plots, respectively) at times indicated in the panels for (a) $\omega_b = 0.5$, (b) $\omega_b = 0.9$, and (c) $\omega_b = 0.95$. The input is the exact sG breather stripe perturbed by a uniformly distributed random perturbation of amplitude 0.01. The domain size corresponds to $|x|, |y| \leq 40$ (only the segment $-13 \leq x \leq 13$ is shown).

it possible to better follow the emergence, evolution, and interactions of the “blobs”.

III. RADIAL BREATHERS

We now turn to the consideration of breathers with axial symmetry, i.e., $u(x, y, t) = u(r, t)$, with $r = \sqrt{x^2 + y^2}$ in a circular domain of radius R . Their existence is suggested by the findings reported in the previous Section, where necking MI splits the sG breather stripe into a chain of persistent

localized modes (“blobs”).

A. Constructing radial breathers

With the aim to construct initial conditions that directly lead to radial breathers, we take, as an input, the exact 1D breather (4), with the x coordinate replaced by the radial one: $u_{\text{radial}}(r, 0) = u_b(r, 0)$. The results are summarized in Figs. 8 and 9, which depict, respectively, isocontours of the energy density, and dynamics and power spectra of the field at the

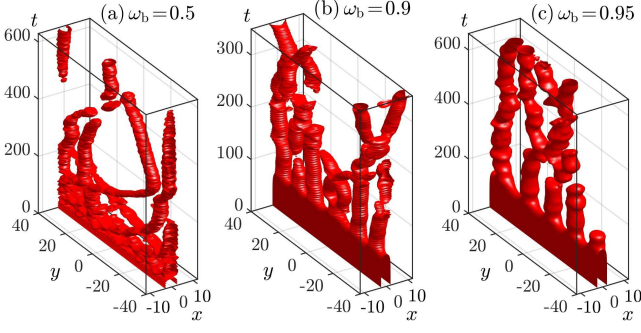


FIG. 7: (Color online) Isocontour plots of the energy density $\mathcal{E}(x, y, t)$ corresponding to the evolution of slightly perturbed sG breather stripes shown in Fig. 6. In all cases, random perturbations added to the initial stripe trigger the development of its transverse MI. As a result, several robust “blobs” emerge, whose motion and interactions dominate subsequent dynamics.

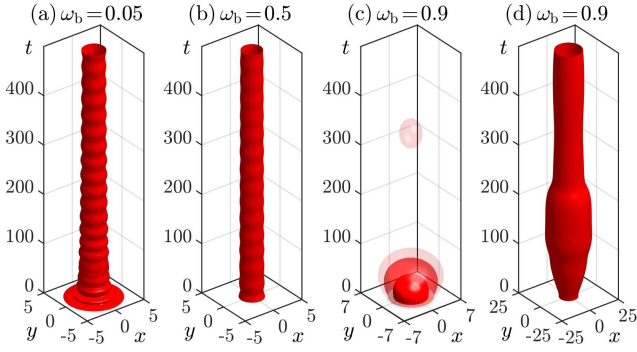


FIG. 8: (Color online) Isocontour plots depicting the evolution of the energy density $\mathcal{E}(x, y, t)$ for radial waveforms initialized by the 1D breather profile, with x replaced by r , for (a) $\omega_b = 0.05$, (b) $\omega_b = 0.5$, and (c)-(d) $\omega_b = 0.9$. The waveforms reshape themselves into radial breathers, which persist over an indefinitely large number of oscillations. In (a) and (b), the isocontour levels correspond to $\mathcal{E}(x, y, t) = \mathcal{E}_0$, with $\mathcal{E}_0 = 2.5$; in (c), three cuts are shown for $\mathcal{E}_0 = 0.1, 0.15$, and 0.3 (more transparent isocontours correspond to smaller \mathcal{E}_0). Apparently, the radial breather for $\omega_b = 0.9$ seems to disperse. However, an isocontour drawn for an even smaller value, $\mathcal{E}_0 = 0.02$, in (d) suggests the presence of a much shallower radial breather.

central point, $u(0, 0, t)$. The results suggest that persistent radial breathers are generated by appropriately crafted inputs. However, the resulting radial breathers do not keep the oscillation frequency corresponding to the one seeded by the initial condition. In fact, for $\omega_b = 0.05$ and $\omega_b = 0.5$, the ensuing radial breathers are very similar (in amplitude and frequency), but they feature an oscillation frequency higher than the one introduced by the input, see green vertical dashed lines in Figs. 9(d)–(f). Note that, as observed in panel (f) of Fig. 9, the input with larger ω_b leads to a much shallower radial breather with a dominant frequency close to 1, i.e., the edge of the phonon band. Similar results were obtained for $\omega_b = 0.75$ and $\omega_b = 0.8$ (not shown here).

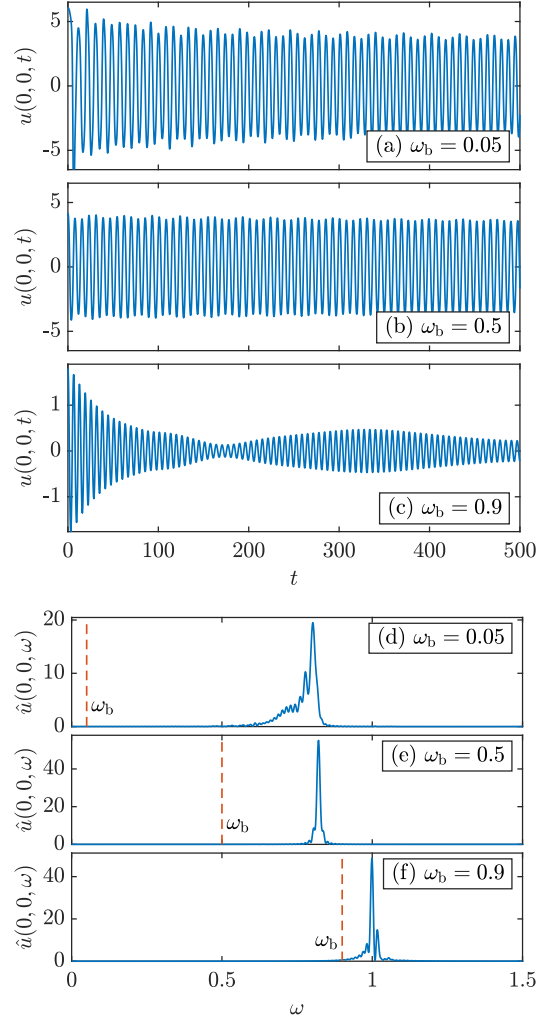


FIG. 9: (Color online) Time series depicting the evolution of field at the central point $u(0, 0, t)$ (top panels) and the corresponding normalized power spectra $\hat{u}(0, 0, \omega)$ (bottom panels), for the cases shown in Fig. 8. For the cases with $\omega_b = 0.05$ (a) and $\omega_b = 0.5$ (b) the resulting radial breathers are very similar in terms of the field amplitude [see plots for $u(0, 0, t)$] and dominant frequency [see plots for $\hat{u}(0, 0, \omega)$]. In panel (c), corresponding to the case with $\omega_b = 0.9$, a much shallower radial breather emerges with a dominant frequency tending to $\omega = 1$, which is the edge of the phonon band. The corresponding dominant frequencies are $\omega \approx 0.8027$ in (a), $\omega \approx 0.8215$ in (b), and $\omega \approx 0.9986$ in (c). Red vertical dashed lines denote frequencies ω_b of the 1D sG breather used as the input.

The numerical experiments shown above might suggest that radial breathers exist as exact solutions. However, on the contrary to the 1D sG equation, its 2D counterpart is not integrable. Therefore, genuine radial breathers cannot exist in the infinite spatial domain, as multiple breathing frequencies, $n\omega$ with $\omega < 1$ but $n > 1/\omega$, resonate with the frequencies belonging to the phonon spectrum, $\omega > 1$, which should give rise to the radiative decay of the breather (only integrable equations make an exception, nullifying the decay rate) [1, 2, 4]. However, in some cases, accurate simu-

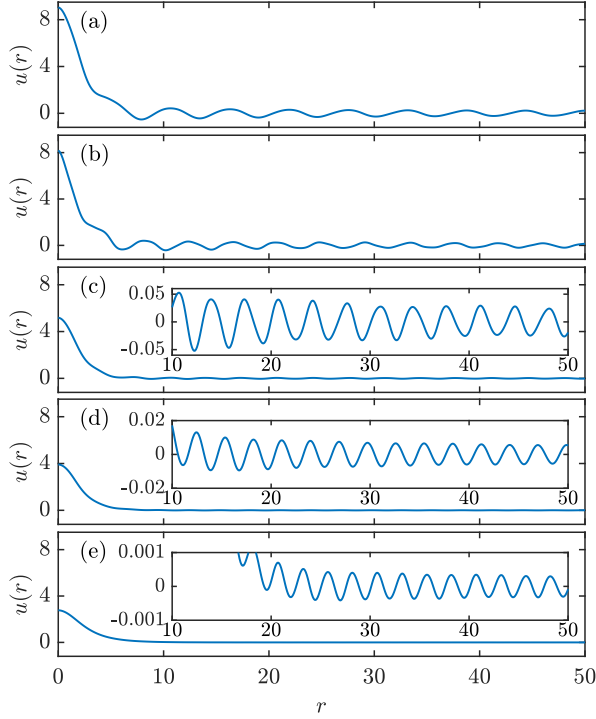


FIG. 10: (Color online) Numerically computed profiles of radial breathers for $\omega_b = 0.5, 0.6, 0.7, 0.8, 0.9$ (from top to bottom). The solution domain is $0 \leq r \leq 200$, only the central portion $r \leq 50$ being shown. All these profiles have oscillatory tails with a small amplitude (see insets for $\omega_b \in 0.7, 0.8, 0.9$).

lations show that the rate of the radiative decay is so small that the 2D sG breathers survive thousands of oscillation periods, with a negligible loss of amplitude [10]. Nevertheless, if the domain is *finite*, there will be gaps in the spectrum, which admit the existence of intraband breathers similar to the *phantom breathers* in discrete lattices introduced in Ref. [30] and feature the aforementioned *nanopteron* wings oscillating in space. For example, we plot in Fig. 10 profiles of numerically exact radial breathers with frequencies $\omega_b = 0.5, 0.6, 0.7, 0.8, 0.9$, computed in the radial domain $0 \leq r \leq 200$ and with zero initial velocity $u_t(r, t = 0) = 0$ (see below for more details of these numerics). As it is made evident by the figure, the radial breathers indeed have distinctive oscillatory tails, which are more prominent for lower values of ω_b , and their amplitude is decaying to zero, in line with the expectation predicted above by the NLS reduction, in the limit of $\omega_b \rightarrow 1$. Indeed, the 2D NLS equation with the cubic self-focusing term creates radial 2D *Townes solitons*; see, e.g., Refs. [31, 32] for a review and Refs. [33, 34] for their experimental realizations, an earlier one in optics and a recently created Townes soliton in atomic gases. Although 1D breathers are also intraband ones and possess a wing in the case of the finite-domain computation, the continuation of 2D radial breathers within the band is a much more subtle problem. A full analysis of the continuation (bifurcation) scenario in the whole range of available frequencies, for which the non-

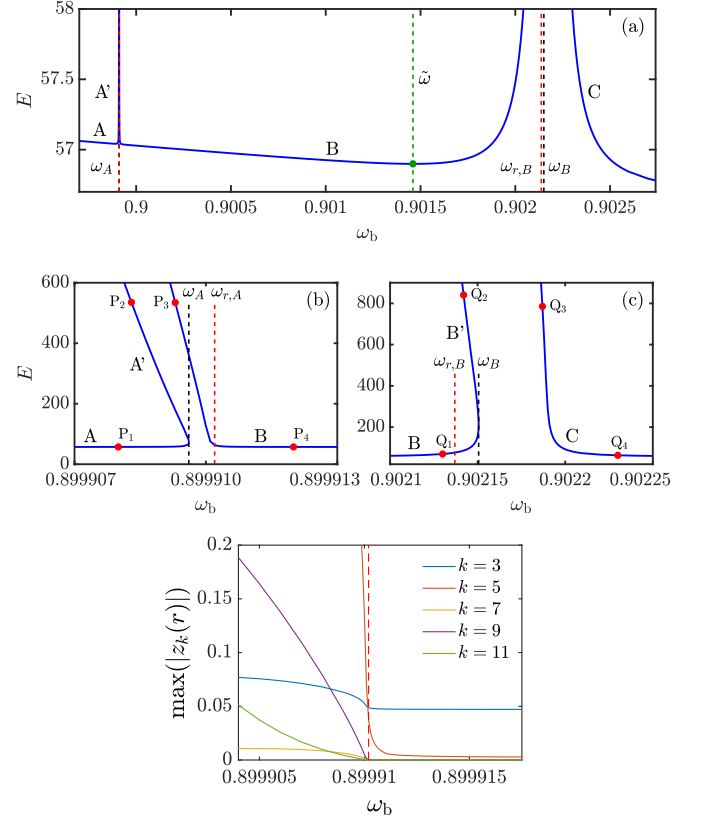


FIG. 11: (Color online) Existence branches of radial breathers for ω_b close to 1. (a–c): Total energy E of radial breathers versus the breather's frequency, ω_b . Panel (a) presents an overview of the different solution branches (see the text), while panels (b) and (c) display zoomed in versions of the transition zones between A-B and B-C branches, respectively. Representative profiles for the solutions belonging to each branch, corresponding to the large red dots, are presented in Figs. 12 and 13. Vertical dashed lines denote the most relevant frequency values: (i) dashed red lines, corresponding to $\omega_{r,A}$ and $\omega_{r,B}$, denote the interval outside of which the breather acquires a minimum at $r = 0$; (ii) dashed black lines, corresponding to ω_A and ω_B , denote the turning points for branches A and B, respectively; (iii) the dashed green line at $\omega_b = \tilde{\omega}$ denotes the location of the energy minimum for branch B, above which the breathers belonging to this branch are prone to exponential instabilities. The bottom panel depicts the maximum amplitude of the main Fourier coefficients of the breathers belonging to branch B. All the computations were performed in region $r \leq R = 200$.

integrability for the 2D equation must play a crucially important role, is outside the scope of the present work. Therefore, in the summary of the stability results that we present below, we focus on branches of radial breathers for large ω_b , *viz.*, $\omega_b > 0.899$, in line with our earlier consideration of the limit of $\omega_b \rightarrow 1$. An advantage of this option is also that, when dealing with larger ω_b , the numerics (performed over one period through the Floquet analysis, see below) are more manageable (faster) than for smaller frequencies.

B. Radial breathers solution branches and stability

We now consider the stability of a “radial breather” $u_b(r, t)$. For this purpose, we proceed as in the breather stripes section. First, we write the PDE (2) in polar coordinates and obtain the equation for the perturbation w corresponding to Eq. (6):

$$w_{tt} - \frac{1}{r}(rw_r)_r - \frac{1}{r^2}w_{\theta\theta} + \cos(u_b(r, t))w = 0. \quad (34)$$

We then assume a solution

$$w(r, \theta, t) = \zeta(r, t) \exp(ik_\theta\theta), \quad (35)$$

with integer angular wavenumber k_θ , yielding the final time-periodic PDE for the perturbation ζ :

$$\zeta_{tt} - \frac{1}{r}(r\zeta_r)_r + \left(\frac{k_\theta^2}{r^2} + \cos(u_b(r, t))\right)\zeta = 0. \quad (36)$$

To deal with the formal singularity of the radial Laplacian at $r = 0$ we do not include this point in the domain so that the closest point to $r = 0$ is $r = h/2$ [that is, $r \in (h/2, R)$], and assume $u_r(r = 0) = 0$. This way of handling the singularity is standard, see for example Ref. [35], and it is equivalent to considering

$$u(r = -h/2) = u(r = h/2). \quad (37)$$

Under this scheme of the spatial discretization, and using zero Dirichlet boundary conditions at $r = R$ (i.e., fixed edges), we employ the standard shooting method in time—implemented by dint of a fourth-order explicit and symplectic Runge-Kutta-Nystrom method developed in Ref. [36], with time step equal to $T/300$ for the shooting method and $T/1500$ for the Floquet analysis (see Appendix)—and seek for periodic solutions, for each given temporal period. Then, for each periodic solution we compute the corresponding stability spectrum via Floquet analysis (see Appendix for details).

To gain insight into the stability (and the ensuing dynamics) of radial (intraband) breathers and their hybridization with phonon modes, we have considered a small interval around $\omega_b = 0.9$. We have verified that for the cases under consideration, where ω_b is close to 1, the Fourier coefficients associated with the breathers decay relatively fast with the increase of their order. This allows us to resolve the solutions with satisfactory resolution. Namely, we have corroborated that increasing the spatial resolution by including more Fourier modes does not lead to any visible change in the obtained stability spectra.

The main stability results for radial breathers with frequencies close to $\omega_b = 0.9$ are summarized in Fig. 11. Specifically, panels (a)–(c) depict the total energy [$E = \iint \mathcal{E} dx dy$, with energy density defined as per Eq. (33)] versus ω_b . Here, three distinct branches (A, B, and C) of the radial branches are found. In analogy to the 1D phantom breathers of Ref. [30], there is branch A to the left, which terminates at a turning point, $\omega_b = \omega_A = 0.89990961$, and central branch B that also finishes at a turning point, $\omega_b = \omega_B = 0.90215058$. Herein, we mostly focus on branch B. Panels (b) and (c) depict

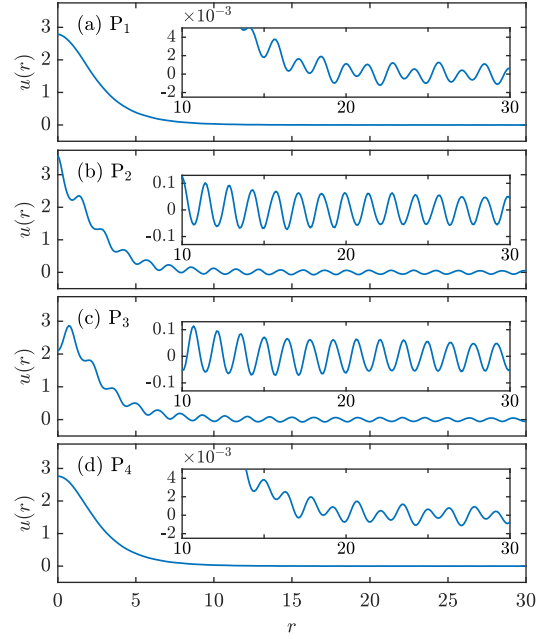


FIG. 12: (Color online). Radial breather’s profiles at the points P_1 , P_2 , P_3 , and P_4 , depicted by large red dots in panel (b) of Fig. 11.

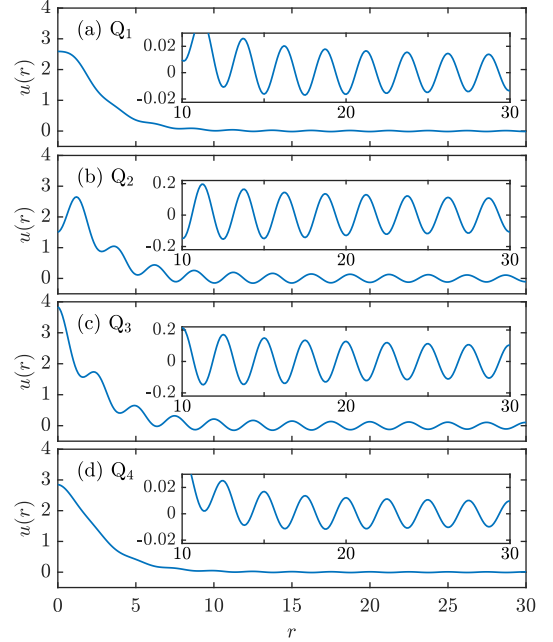


FIG. 13: (Color online). Radial breather’s profiles at the points Q_1 , Q_2 , Q_3 , and Q_4 , depicted by large red dots in panel (c) of Fig. 11.

zoomed areas from (a) around the frequencies where, respectively, branch A turns and branch B starts, or branch B turns and branch C starts. These two bifurcations occur, due to the resonance of the *seventh harmonic* of the ω_b with phonons, respectively, at points $\omega_{\text{phonon}}/7 = \omega_b^A = 0.8999686$ and $\omega_{\text{phonon}}/7 = \omega_b^B = 0.902735$. These phonon frequencies

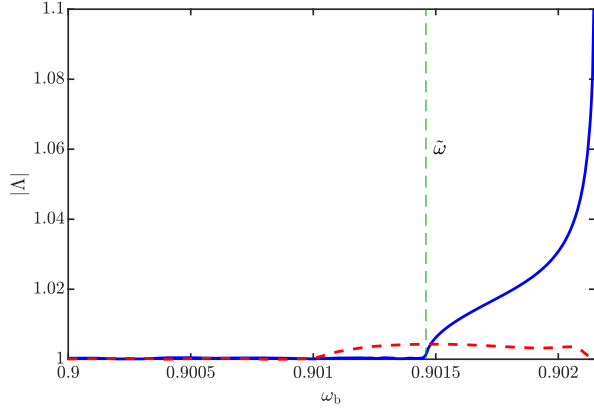


FIG. 14: (Color online) Largest Floquet multipliers for $k_\theta = 0$ (the solid blue line) and $k_\theta = 1$ (the red dashed line) for breathers belonging to branch B. The strongest instability, which takes place at $\omega_b > \tilde{\omega} = 0.90146$, is exponential (monotonously growing), other instabilities being oscillatory.

produce, via the dispersion relation (16), the wavenumber observed in the tails of the breather, confirming that the resonance between the breather and phonons takes place. The left and central branches join, via turning points, through additional solution branches (A' and B', respectively, see Fig. 11).

Note that breathers belonging to branch B-B' have the amplitude maximum displaced from $r = 0$ (that is, the solutions are shaped as *ring breathers*) at $\omega_b < \omega_{r,A} = 0.8999102$ and $\omega_b > \omega_{r,B} = 0.902137$. Indeed, Figs. 12 and 13 display the breather's profiles—again for zero initial velocity $u_t(r, t = 0) = 0$ —close to the transitions between branches, *viz.*, respectively, $A \rightleftharpoons B$ and $B \rightleftharpoons C$, and, specifically, in panel (c) of Fig. 12 and panel (b) of Fig. 13, the profiles do not have a maximum at $r = 0$. This qualitative change of the breathers' shape can be understood by noting that, as mentioned above, the seventh harmonic of these breathers is resonant with phonon waves, its amplitude being $\simeq 0.1$ times the amplitude of the fundamental (first) harmonic. As a consequence, the breather progressively resembles a delocalized phonon wave when the frequency is decreased. Thus, the rings in the breather's shape at $\omega_b < \omega_{r,A}$ are a consequence of the hybridization with phonons.

Finally, we address the stability of the radial breather solutions. Our numerical Floquet stability analysis suggests that the breathers belonging to branch B are mainly affected by radial perturbations, *i.e.*, those with $k_\theta = 0$ in Eq. (35), and that the only exponential instabilities that occur are related to the existence of minima in the energy-vs.-frequency dependence, *i.e.*, ones of the kind predicted in Ref. [37]. Because of this, breathers belonging to branch B in Fig. 11 are subject to exponential instability at $\omega_b > \tilde{\omega} = 0.90146$, where $\tilde{\omega}$ is the energy-minimum point on B branch, denoted by the vertical green dashed line in the figure. The full stability spectrum for the radial-breather solutions in branch B is shown in Fig. 14. As expected, the breather becomes exponentially unstable to radial perturbations (see the solid blue line representing the

FM corresponding to radial perturbations) at $\omega_b > \tilde{\omega}$. In addition, the breathers belonging to this branch are also subject to an oscillatory instability at $\omega_b > 0.8999095$, although its magnitude is small ($|\Lambda| \lesssim 1.005$). We have checked that this weak oscillatory instability is not a numerical artifact, as changing k_m [controlling the number of Fourier modes, per Eq. (41)] or the integration step in the Floquet analysis do not alter the spectrum. Changing the discretization parameter would also lead to the appearance of new phonon modes and, at the same time, new resonances that would change the existence interval of the radial breathers. In any case, these weak oscillatory instabilities should not have a noticeable effect on the breathers' dynamics. The oscillatory instabilities were only found for $k_\theta = 1$ in Eq. (35). The breathers belonging to branch B' are exponentially unstable against the perturbations with $k_\theta = 0$ at all values of ω_b , and feature weak oscillatory instabilities for $k_\theta \geq 1$. A brief exploration of the stability for breathers belonging to branch A indicates that the results are very similar to those reported here for branch B.

IV. CONCLUSIONS

We have studied the extension of sG breathers to 2D, in the form of quasi-1D breather stripes and localized radial breathers. Starting from the long-wave MI (modulational instability) of the stripe, discovered in the seminal work by Ablowitz and Kodama [17] and confirmed herein, we have expanded the MI analysis to arbitrary wavelengths of the transverse perturbations. In the limit of small-amplitude broad breathers, with frequency $\omega_b \rightarrow 1$, we have employed the asymptotic multiscale expansion method to match the dynamics of the breather stripes to that of bright soliton stripes in the framework of the 2D NLS equation. Perhaps more importantly, we have developed a novel version of the VA (variational approximation), whereby the 2D dynamics of the sG breather stripe is reduced to a filament-type evolution equation for the amplitude of the breather along the stripe. The VA allowed us to formulate an approximate reduced model that not only captures the necking MI (*i.e.*, the dependence of the MI gain on the perturbation wavenumber), but is also able to predict the dynamics beyond the linear instability setting, and up to close to the breakup of the stripe by the growing necking perturbations.

It is precisely the necking MI of sG breather stripes that results in the nucleation of temporally oscillatory, spatially localized “blobs” in the form of radial breathers. Numerical results demonstrate that the blobs can collide or merge with nearby ones. The apparent robustness of these modes has prompted us to study their existence and stability in more detail. It is important to note that, contrary to the 1D sG equation, its 2D counterpart is not integrable, hence genuine radial breathers cannot exist in infinite domains for infinitely long times due to resonances of multiple harmonics of the breather with the phonon (continuous) spectrum. Nonetheless, in the finite domain it is possible to find intraband breathers, similarly to how it was done for 1D *phantom breathers* that were discovered in Ref. [30]. In fact, our results show that such in-

traband radial breathers, possessing a “nanopterion” spatially oscillatory tail, do exist and may be stable in the finite domain. The full bifurcation structure of such radial breathers with arbitrary values of the oscillation frequency, ω_b , is quite complex. Nonetheless, we have performed a detailed numerical study for the existence of broad small-amplitude radial breathers for ω_b close to 1, in the vicinity of some of the underlying resonances. We have identified several solution branches and their stability, by means of numerical Floquet analysis, finding that such breathers may indeed be stable in the finite domain.

There are numerous avenues deserving further study. For instance, a more complete characterization of the bifurcation scenarios for arbitrary values of ω_b may be able to elucidate further nontrivial bifurcations and destabilization scenarios. Also, the dynamics and interactions of radial breathers clearly merit further study: for instance, a challenging objective is to investigate the outcome of interactions between radial breathers (including collisions between moving ones), as a function of their relative phase, velocity, and frequencies. Lastly, it is natural to generalize the consideration for 3D settings, and examine whether spherically symmetric radial breathers may survive in a finite domain, and/or whether they may be produced spontaneously via MI of quasi-2D breather planes embedded in 3D. These topics are presently under consideration, and results will be reported elsewhere.

Acknowledgments

This material is based upon work supported by the US National Science Foundation under Grants PHY-1602994 and DMS-1809074 (P.G.K.). P.G.K. also acknowledges support from the Leverhulme Trust via a Visiting Fellowship and thanks the Mathematical Institute of the University of Oxford for its hospitality during this work. R.C.G. gratefully acknowledges support from the US National Science Foundation under Grant PHY-1603058. J.C-M. was supported by project P18-RT-3480 (Regional Government of Andalusia). B.A.M. appreciates support provided by Israel Science Foundation through grant Np. 1286/17.

Appendix: Numerical implementation for periodic states and their Floquet stability analysis

In this Appendix, we outline the Floquet analysis that was deployed for quasi-1D breathers embedded in rectangular domains and radial breathers in circular domains. These breathers are T -periodic solutions corresponding to steady states of the dynamics after time evolves from $t = 0$ to $t = T$. Furthermore, as these solutions only depend (non-trivially) on a single spatial coordinate—the x - or r -direction for stripe and radial breathers respectively—they can be numerically computed as 1D solutions along this longitudinal direction. Nonetheless, it is crucial to note that the stability for these solutions has to be computed in the *full* 2D domain where these breather structures are embedded in. Namely, perturba-

tions to these solutions need to be followed, not only along the longitudinal direction, but more importantly, along the transverse direction. To this end, as described below, we follow the growth of plane-wave *transverse* perturbations with wavenumbers k_y and k_θ , along the y - and θ -directions for, respectively, the breather stripes in the Cartesian plane and radial breathers in polar coordinates. Thus, each wavenumber, k_y or k_θ , yields a 1D perturbation equation determining the stability of the corresponding modulations over one period T that is treated, as detailed below, using Floquet analysis to obtain its corresponding eigenvalues (eigenfrequencies) and eigenvectors (eigenmodes).

The first step in our numerical computations is to discretize in space the solution and its corresponding derivatives. To this end, we consider a finite-difference scheme with a (spatial) discretization parameter $h = 0.1$, which transforms the PDE for $u(x, t)$ into a set of N coupled ODEs for $u_n \equiv u(x_n, t)$ on the discrete grid $\{x_n\}$. The discretized version of the quasi-1D sG equation (also known as the Frenkel-Kontorova model) reads:

$$\ddot{u}_n + \sin(u_n) + \frac{1}{h^2}(u_{n+1} - 2u_n + u_{n-1}) = 0, \quad (38)$$

where $n = -N/2 \dots N/2$. Similarly, for the radial breather the corresponding discretized radial sG equation may be written as

$$\ddot{u}_n + \sin(u_n) + \frac{1}{h^2}(u_{n+1} - 2u_n + u_{n-1}) + \frac{1}{2nh^2}(u_{n-1} - u_{n+1}), n = 1 \dots N \quad (39)$$

To produce breathers in the numerical form, we have made use of two different techniques, based on the fact that the solutions are T -periodic, with $T = 2\pi/\omega_b$: (i) a shooting method, based on the consideration of the map,

$$\mathbf{Y}(0) \rightarrow \mathbf{Y}(T), \quad \mathbf{Y}(t) = \begin{bmatrix} \{u_n(t)\} \\ \{\dot{u}_n(t)\} \end{bmatrix}, \quad (40)$$

and (ii) a Fourier-transform implementation, based on expressing the solution of the discretized dynamical equations in the form of a truncated Fourier series:

$$u_n(t) = z_{0,n} + 2 \sum_{k=1}^{k_m} z_{k,n} \cos(k\omega t), \quad (41)$$

with k_m being the maximum of the absolute value of the k in our truncation of the full Fourier series. In the numerics, $k_m = 11$ was chosen. Note that the spatial evenness of the sG potential [$V(u) = 1 - \cos(u)$], the Fourier coefficients with even k are zero and, consequently, only odd harmonics of ω_b can resonate with phonons.

After the introduction of Eq. (41) in the dynamical equations, one gets a set of $N \times (k_m + 1)$ nonlinear, coupled algebraic equations. For a detailed explanation of these methods, the reader is referred to Refs. [38, 39]. In both methods, the continuation in the frequency is implemented via the path-following (Newton-Raphson) method. The Fourier-transformed methods have the advantage, among others, of

providing an explicit analytical form of the Jacobian, which makes the calculations faster. However, for frequencies smaller than ~ 0.6 , the Fourier coefficients decay slowly and a large number of coefficients should be kept to produce an accurate solution, which makes the Jacobian numerically expensive. Because of this, we developed the analysis based on method (i) to quasi-1D breathers in the range $0.1 \leq \omega_b < 1$, whereas the Fourier-transform methods (ii) were applied to the radial breathers, when we focused on frequencies around $\omega_b = 0.9$.

To study the spectral stability of the breathers, we introduce a small perturbation $\xi_n(t)$ to a given solution $u_{n,0}(t)$ of the discretized dynamical equations as $u_n(t) = u_{n,0}(t) + \xi_n(t)$ [8]. Then, defining the perturbation as $\xi_n = \xi_{x,n} \exp(ik_y y)$ in the quasi-1D breather stripe case yields

$$\ddot{\xi}_{x,n} + [\cos(u_n) + k_y^2] \xi_{x,n} + \frac{1}{h^2} (\xi_{x,n+1} - 2\xi_{x,n} + \xi_{x,n-1}) = 0.$$

On the other hand, for the radial breather the corresponding dynamics for the perturbation may be written as

$$\ddot{\zeta}_{r,n} + \left[\cos(u_n) + \frac{k_\theta^2}{n^2 h^2} \right] \zeta_{r,n} + \frac{1}{h^2} (\zeta_{r,n+1} - 2\zeta_{r,n} + \zeta_{r,n-1}) + \frac{1}{2nh^2} (\zeta_{r,n-1} - \zeta_{r,n+1}) = 0,$$

as $\zeta_n = \zeta_{r,n} \exp(ik_\theta \theta)$. Due to the (temporal) periodicity of the solutions, Floquet analysis must be employed. In such a case, the stability properties are determined by the spectrum of the Floquet operator \mathcal{M} (whose matrix representation is the monodromy), defined as:

$$\begin{pmatrix} \{\xi_n(T)\} \\ \{\xi_n(0)\} \end{pmatrix} = \mathcal{M} \begin{pmatrix} \{\xi_n(0)\} \\ \{\xi_n(0)\} \end{pmatrix}, \quad (42)$$

for the perturbation ξ_n in the quasi-1D breather stripe case and an identical equation for ζ_n for the radial breather case. The $2N \times 2N$ monodromy eigenvalues $\Lambda \equiv \exp(i\Theta)$ are dubbed the FMs (Floquet multipliers), with *Floquet exponents* (FEs) Θ . A consequence of the fact that the Floquet operator is real is that, if Λ is an FM, Λ^* is an FM too. Further, because of the symplecticity of the Floquet operator, $1/\Lambda$ is also an FM. In other words, FMs always come in quadruplets $(\Lambda, \Lambda^*, 1/\Lambda, 1/\Lambda^*)$ if the monodromy eigenvalues are complex, and in pairs $(\Lambda, 1/\Lambda)$ if the eigenvalues are real. As a consequence, a necessary and sufficient condition for a breather to be linearly stable is that Θ must be real (i.e., that the corresponding FMs lie on the unit circle in the complex plane). Finally, note that FMs Λ are related to eigenvalues λ through relation $\Lambda = \exp(\lambda T)$.

-
- [1] R. K. Dodd, J. C. Eilbeck, J. D. Gibbon, and H. C. Morris, *Solitons and Nonlinear Wave Equations*, Academic Press (London, 1982).
 - [2] Th. Dauxois and M. Peyrard, *Physics of Solitons*, Cambridge University Press (Cambridge, 2006).
 - [3] J. Cuevas, P. G. Kevrekidis, and F. L. Williams (Eds.), *The sine-Gordon Model and its Applications: From Pendula and Josephson Junctions to Gravity and High Energy Physics*, Springer-Verlag (Heidelberg, 2014).
 - [4] Yu. S. Kivshar and B. A. Malomed, *Rev. Mod. Phys.* **61**, 763 (1989).
 - [5] C. Rogers and W. K. Schief, *Bäcklund and Darboux transformations* (Cambridge University Press: Cambridge, 2002).
 - [6] M. J. Ablowitz, D. J. Kaup, A. C. Newell, and H. Segur, *Phys. Rev. Lett.* **30**, 1262 (1973).
 - [7] S. Flach and A. Gorbach, *Discrete breathers – Advances in theory and applications*, *Phys. Rep.* **467**, 1 (2008).
 - [8] S. Aubry, *Phys. D* **103**, 201 (1997).
 - [9] P. L. Christiansen and O. H. Olsen, *Phys. Scr.* **20**, 531 (1979); *Phys. Lett. A* **68**, 185 (1978); P. S. Lomdahl, O. H. Olsen, and P. L. Christiansen, *Phys. Lett. A* **78**, 125 (1980); P. L. Christiansen and P. S. Lomdahl, *Phys. D* **2**, 482 (1981).
 - [10] J. Geicke, *Phys. D* **4**, 197 (1982); *Phys. Scr.* **29**, 431 (1984); *Phys. Lett. A* **98**, 147 (1983).
 - [11] I. L. Bogolubsky and V. G. Makhankov, *JETP Lett.* **24**, 12 (1976).
 - [12] M. R. Samuelsen, *Phys. Lett. A* **74**, 21 (1979).
 - [13] J.-G. Caputo and M. P. Soerensen, *Phys. Rev. E* **88**, 022915 (2013).
 - [14] P. G. Kevrekidis, I. Danaila, J.-G. Caputo, and R. Carretero-González, *Phys. Rev. E* **98**, 052217 (2018).
 - [15] E. G. Fedorov, A. V. Zhukov, R. Bouffanais, B. A. Malomed, H. Leblond, D. Mihalache, N. N. Rosanov, M. B. Belonenko, and T. F. George, *Opt. Express* **27**, 27592 (2019).
 - [16] E. M. Maslov, *Physica D* **15**, 433 (1985).
 - [17] Y. Kodama and M. J. Ablowitz, *J. Math. Phys.* **21**, 928 (1980).
 - [18] Yu. S. Kivshar and D. E. Pelinovsky, *Phys. Rep.* **331**, 117 (2000).
 - [19] E. A. Kuznetsov and S. K. Turitsyn, *Zh. Eksp. Teor. Fiz.* **94**, 119 (1988) [*Sov. Phys. JETP* **67**, 1583 (1988)].
 - [20] B. P. Anderson, P. C. Haljan, C. A. Regal, D. L. Feder, L. A. Collins, C. W. Clark, and E. A. Cornell, *Phys. Rev. Lett.* **86**, 2926 (2001).
 - [21] V. Tikhonenko, J. Christou, B. Luther-Davies, and Yu. S. Kivshar, *Opt. Lett.* **21**, 1129 (1996).
 - [22] S.-P. Gorza, B. Deconinck, Ph. Emplit, T. Trogdon, and M. Haelterman, *Phys. Rev. Lett.* **106**, 094101 (2011).
 - [23] J. Cuevas-Maraver and P. G. Kevrekidis, in *A dynamical perspective on the ϕ^4 model. Past, present and future*, P. G. Kevrekidis and J. Cuevas Maraver (eds.) (Springer, Cham, 2019).
 - [24] L. A. Cisneros-Ake, R. Carretero-González, and P. G. Kevrekidis, *Phys. Rev. Research* **1**, 033043 (2019).
 - [25] J. Yang, *Nonlinear waves in integrable and nonintegrable systems*, Society for Industrial and Applied Mathematics (2010).
 - [26] A. Jeffrey and T. Kawahara, *Asymptotic Methods in Nonlinear Wave Theory*, Pitman, London (1982).
 - [27] E. A. Kuznetsov, A. M. Rubenchik, and V. E. Zakharov, *Phys. Rep.* **142**, 103 (1986).
 - [28] S.-P. Gorza, P. Kockaert, Ph. Emplit, and M. Haelterman, *Phys. Rev. Lett.* **102**, 134101 (2009).
 - [29] B. A. Malomed, *Progr. Optics* **43**, 71 (2002).
 - [30] A. M. Morgante, M. Johansson, S. Aubry, and G. Kopidakis, *J. Phys. A: Math. Gen.* **35**, 4999 (2002).
 - [31] G. Fibich, *The Nonlinear Schrödinger Equation: Singular Solutions and Optical Collapse* (Springer: Heidelberg, 2015).

- [32] B. A. Malomed, Eur. Phys. J. Special Topics **s225**, 2507 (2016).
- [33] K. D. Moll and A. L. Gaeta, in *Nonlinear Optics: Materials, Fundamentals and Applications*, A. Sawchuk (ed.) (Optical Society of America, 2002).
- [34] Cheng-An Chen and Chen-Lung Hung, arXiv:1907.12550 (2019).
- [35] H. Sakaguchi and B. A. Malomed, Phys. Rev. E **101**, 012211 (2020).
- [36] M.P. Calvo and J.M. Sanz-Serna, SIAM J. Sci. Comp. **14** 936 (1993).
- [37] P. G. Kevrekidis, J. Cuevas-Maraver, and D. E. Pelinovsky, Phys. Rev. Lett. **119**, 094101 (2016).
- [38] J. F. R. Archilla, R. S. MacKay, and J.L. Marín, Phys. D **134**, 406 (1999).
- [39] J. L. Marín and S. Aubry, Nonlinearity **9**, 1501 (1996).